Optics and Laser Technology 93 (2017) 49–59

Contents lists available at ScienceDirect

Optics and Laser Technology

journal homepage: www.elsevier.com/locate/jolt

Full length article

Laser cutting sandwich structure glass–silicon–glass wafer with laser induced thermal–crack propagation

Yecheng Cai [a], Maolu Wang [a], Hongzhi Zhang [a], Lijun Yang [a], Xihong Fu [b], Yang Wang [a,*]

[a] Department of Aeronautics and Astronautics Manufacturing Engineering, School of Mechatronics Engineering, Harbin Institute of Technology, Harbin, Heilongjiang 150001, China
[b] State Key Laboratory of Luminescence and Applications, Changchun Institute of Optics, Fine Mechanics and Physics, Chinese Academy of Sciences, Changchun, Jilin 130033, China

ARTICLE INFO

Article history:
Received 13 June 2016
Received in revised form 18 October 2016
Accepted 24 January 2017
Available online 23 February 2017

Keywords:
Silicon-glass device
1064 nm semiconductor laser
Laser induced thermal-crack propagation (LITP)
J-integral
Crack propagation profile

ABSTRACT

Silicon-glass devices are widely used in IC industry, MEMS and solar energy system because of their reliability and simplicity of the manufacturing process. With the trend toward the wafer level chip scale package (WLCSP) technology, the suitable dicing method of silicon-glass bonded structure wafer has become necessary. In this paper, a combined experimental and computational approach is undertaken to investigate the feasibility of cutting the sandwich structure glass-silicon-glass (SGS) wafer with laser induced thermal-crack propagation (LITP) method. A 1064 nm semiconductor laser cutting system with double laser beams which could simultaneously irradiate on the top and bottom of the sandwich structure wafer has been designed. A mathematical model for describing the physical process of the interaction between laser and SGS wafer, which consists of two surface heating sources and two volumetric heating sources, has been established. The temperature stress distribution are simulated by using finite element method (FEM) analysis software ABAQUS. The crack propagation process is analyzed by using the J-integral method. In the FEM model, a stationary planar crack is embedded in the wafer and the J-integral values around the crack front edge are determined using the FEM. A verification experiment under typical parameters is conducted and the crack propagation profile on the fracture surface is examined by the optical microscope and explained from the stress distribution and J-integral value.

1. Introduction

Recent experiences from MEMS, IC and solar power industries have clearly demonstrated the critical importance of silicon-glass devices. In the device package procedure, the glass wafer and the silicon wafer are joining together using anodic bonding technology which could provide high reliability, stability and hermetic sealing. And borosilicate glass, such as Pyrex or Borofloat, which has a lower coefficient of thermal expansion, is used [1]. Most of these devices have been using silicon-glass double layer structure [2,3]. However, in some peculiar application occasions, glass-silicon-glass (SGS) sandwich structure has also been adopted [4,5]. Typically, the wafer level chip scale package (WLCSP) technology has been used in the fabrication of the silicon-glass devices [6]. And the dicing process is carried out after the wafer bonding process. So the significance of developing a suitable dicing method for SGS wafer has become obvious.

There are a number of dicing methods available for glass and silicon respectively. Most of them could fall into the category of mechanical dicing or laser dicing. At present, three major basic dicing methods are being used in semiconductor industry: the diamond blade cutting method [7]; the laser melting and evaporation cutting method [8–11]; the laser induced thermal-crack propagation (LITP) method [12].

LITP has proven effective in separating FPD glass substrate [13–19] as well as many other kinds of brittle materials (e.g. silicon [20–22], ceramic [23], etc.). This method uses laser to heat up the sheet locally and cause non-uniform thermal expansion, which would generate a specific tensile-compressive thermal stress field that controls the crack propagation process. Compare to other methods, this method, especially the full body separation with LITP method, could separate the sheet without material removal and generate a perfect fracture surface without microcracks and defects.

Up until now, due to the complexity of the thermal crack propagation mechanism, most studies concerning LITP method were focused on the cutting problems of single material sheet of single

* Corresponding author at: Dept. of Aeronautics and Astronautics Manufacturing Engineering, School of Mechatronics Engineering, Manufacturing Building 525, PO Box 422, Harbin Institute of Technology, No. 92, XiDaZhi Street, NanGang District, Harbin, Heilongjiang 150001, China.

E-mail addresses: cyclxoath@outlook.com (Y. Cai), maoluwang@sina.com (M. Wang), zhz-hit@163.com (H. Zhang), yljtj@hit.edu.cn (L. Yang), fuxh@ciomp.ac.cn (X. Fu), tsailxoath@outlook.com (Y. Wang).

http://dx.doi.org/10.1016/j.optlastec.2017.01.028
0030-3992/

layer or multilayer (not bonded together). However in practical applications, the device is usually characterized as multilayers structure of various kinds of materials which are bonded together and affected each other, for instance, the anodically bonded silicon-glass multilayer sheet. In previous studies, several solutions have been proposed for cutting anodically bonded silicon-glass multilayer sheet, such as fabricating a recess beneath the dicing line [24], using a combination of the ultrafast laser stealth dicing method and the LITP method [25,26], and full body LITP method [27]. The first solution requires extra processing step of grooving for the recesses. And the second solution requires dedicated multi-laser system which consists three types of lasers with different wavelengths and pulse-durations for each dicing steps. By comparison, the full body LITP method is a very promising solution, which only requires one types of laser with one clean and efficient processing step of cutting. In paper [27], the mechanism of cutting silicon-glass double layer wafer using full body LITP method was studied using an integrated experimental/analytical approach. During the cutting process, 79.6% of the 1064 nm laser energy were absorbed at the inner bonding surface of the silicon layer, and the crack front edge is a curve which starts at the bottom surface of the silicon layer, then crosses the interface, and finally ends at the top surface of the glass layer. Both layers were separated at once scanning process.

Inferring from the silicon-glass double layer wafer LITP method cutting mechanism, we reasoned that the SGS wafer would also be separated at once scanning process. Therefore in this paper, the authors attempted to set up a double laser beam cutting system to achieve full-body separation of the anodic bonded SGS wafer using LITP method. A FEM model with stationary crack was built and the fracture parameter J-integral wass chosen to analyze the crack propagation process. A feasibility experiment was conducted using moderate cutting parameters.

2. Experimental methods

A 1064 nm semiconductor laser cutting system with double laser beams which could simultaneously irradiate on the top and bottom of the sandwich structure wafer has been designed.

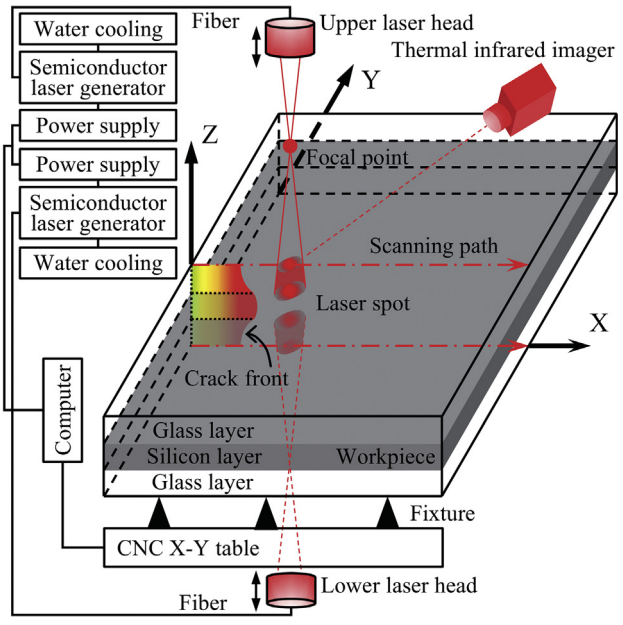

Fig. 1. Schematic diagram of the experimental setup.

As Figs. 1 and 2 illustrate, the system consists of two independent control laser sources, a horizontal x-y table, and a computer to control the CNC system. Two laser beams irradiate vertically on the top and bottom of the specimen. Both lasers are 300 W fiber-optic-coupled continuous semiconductor laser, and emitting at 1064 nm with TEM 00 beam mode. Each laser has an independent generator, together with the water cooling unit and the power supply unit. A horizontal fine adjustment device is installed to adjust the x and y position of the upper laser head and keep the two laser beams coaxial and symmetrical about the specimen. Both laser heads could move along the Z-axis driven by two independent motors. The computer controls the movement of X-axis and Y-axis of the x-y table, the movement of Z-axis of both laser heads, and the laser parameters through customized software. Further detailed specifications concerning the experimental setup are given in Table 1. A thermal infrared imager (FLIR) is arranged for measuring temperature.

The sandwich structure wafer, which is manufactured by anodic bonded a silicon wafer (n-type with (1 0 0) crystal plane with both surfaces polished) to two Borofloat 33 (BF33) borosilicate glass wafers (produced by Schott) on both sides of the silicon wafer. The specimen has a total thickness of 1.5 mm (0.5 + 0.5 + 0.5 mm) and a diameter of 101.6 mm (4 in.). An initial through thickness notch serving as the source fracture is incised on the leading edge with a diamond wire saw.

The fracture surface is inspected by the optical microscope (Zeiss) and scanning electron microscope (FEI Quanta). The fracture surface profile is measured using surface profilers (Taylor Hobson).

3. Numerical analysis

The temperature stress distribution of the specimen and the J-integral along the crack front in cutting process are calculated by using the FEM software ABAQUS. The non-steady sequentially coupled heat transfer and thermal stress analysis is adopted. Fig. 3 shows the flow chart of the simulation process.

General mesh geometry of the specimen is shown in Fig. 4. A stationary seam-type crack is placed at y = 0 on the scanning path with crack front edge set at x = 5 mm. In order to achieve high accuracy in the calculation of J-integral of the crack, mesh adjacent to the crack front region is reconstructed in X, Y, and Z directions and refined, as shown in Fig. 5. The minimum element width in the X-direction is 50 nm, and the minimum element depth in the z-direction is 15.6 μm. The total number of nodes is 327,159 and the total number of elements is 251,418.

Based on the theoretical model established in the previous study [27], the 1064 nm laser beam transmitted through the whole glass layer and then is absorbed on the surface of the silicon layer. Fig. 6 shows the thermal loads symmetrically applies on the specimen. There are two volumetric heating sources loaded in both glass layers and two surface heating sources loaded on the top and bottom surface of the silicon layer. The optical properties of the specimen under 1064 nm laser radiation are given in Table 2 [27].

Both lasers use the identical cutting paramters. The laser is modeled by applying the planar circular Gaussian heat flux. And the attenuation and divergence of laser in the glass layer is also considered. The heat flux in the upper glass layer could be described as Eq. (1). And for the lower glass layer, the formulation is similar to Eq. (1), except all of the ($3H$-z) terms in the expression should be replaced with z. The heat flux on the top and bottom surface of the silicon layer could be expressed as Eq. (2). In these equations, q_G is volume heat intensity, q_S is surface heat intensity, I is the laser power, $R_{\Delta G}$ is the air-glass interface reflectivity, α is the

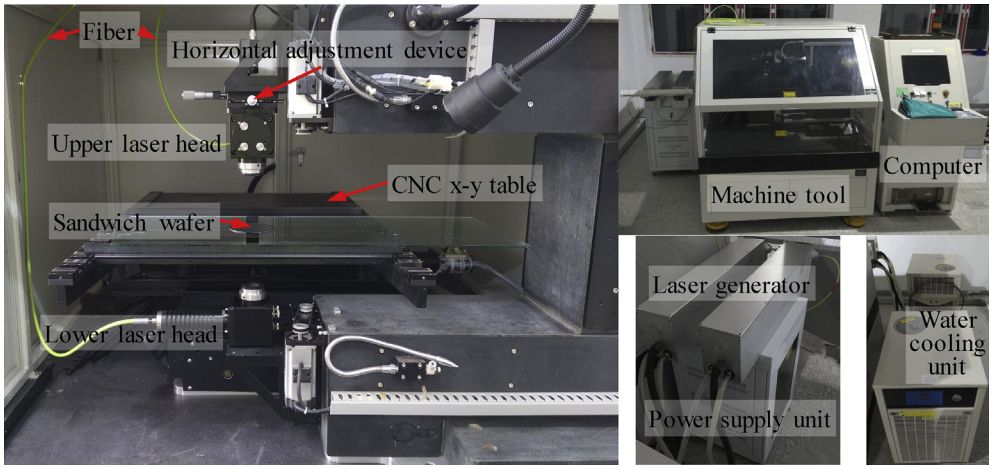

Fig. 2. Photographs of the experimental setup.

Table 1
Specifications for double lasers cutting machine tool.

X/Y-axis	Movement stroke [mm]	500
	Cutting speed [mm/s]	0.1–200
	Positioning accuracy [mm]	±0.02
Z-axis	Movement stroke [mm]	50
	Resolution [mm]	0.01
Horizontal adjustment device	Movement stroke [mm]	10
	Accuracy [mm]	0.005

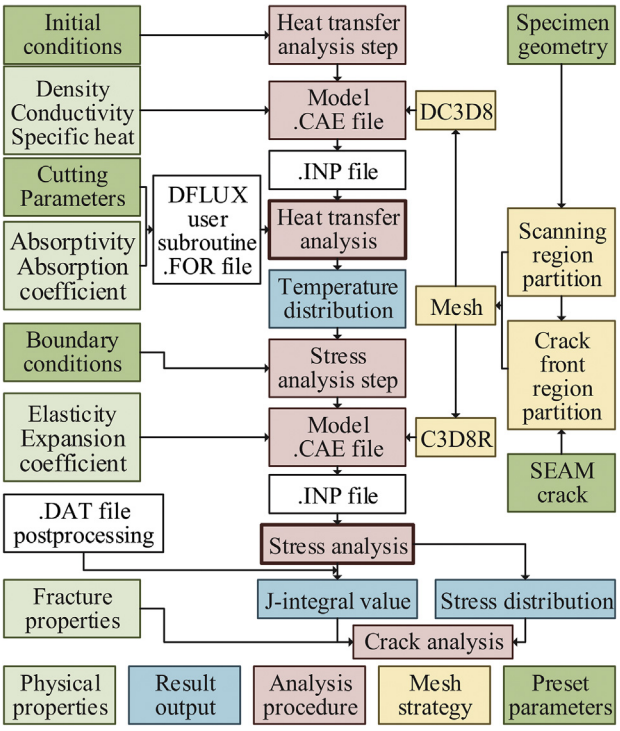

Fig. 3. The flow chart of the simulation process.

absorption coefficient, η_S is the absorptivity of the silicon layer, $3H$ is the whole thickness of the specimen ($H = 0.5$ mm), v is the laser scanning velocity, θ is the divergence angle of laser beam, r_G is the spot radius on top/bottom surface of the upper/lower glass layer, r_S is the spot radius on top/bottom surface of the silicon layer, v is the scanning speed, x_0 and y_0 are the coordinates of the starting point of the scanning process.

$$q_G(x,y,z) = \frac{2(1-R_{AG})\alpha I}{\pi[r_G-(3H-z)\tan\theta]^2} e^{-\alpha(3H-z)} e^{-2\frac{(x-x_0-vt)^2+(y-y_0)^2}{[r_G-(3H-z)\tan\theta]^2}} \quad (1)$$

$$q_S(x,y) = \frac{2\eta_S I}{\pi r_S^2} e^{-2\frac{(x-x_0-vt)^2+(y-y_0)^2}{r_S^2}} \quad (2)$$

The user subroutine DFLUX is used to define the distributed volume heat flux and the surface heat flux according to Eqs. (1) and (2). Initial room temperature T_0, is set at 18 °C. Element type use the DC3D8 element.

In order to further understand and analyze the crack propagation process, the J-integral value is calculated additionally in the thermal stress analysis step. The J-integral, which was proposed by Rice [28] and has been used as a fracture mechanics parameter in many engineering applications, is known as the path-independent contour integral representing the energy release rate at the crack front. Within linear elastic fracture mechanics (LEFM), according to the Griffith's crack energy balance criterion, the K-G equivalence relationship and the J-integral theory, for plane stress mode I critical equilibrium state crack, critical condition of the crack propagation could be expressed as [29]

$$J_c = G_c = \frac{K_{Ic}^2}{E} = R_0 = 2\gamma \quad (3)$$

$$K_{Ic} = T_0 = \sqrt{ER_0} \quad (4)$$

where J_0 is the critical J-integral value, G_0 is the critical energy release rate, K_{Ic} is the critical stress intensity factor, E is Young's module, R_0 is crack resistance force, γ is surface energy, and T_0 is fracture toughness. Since the stress analysis step is quasi-static fracture analysis, the J-integral could be calculated to characterize the energy release associated with crack growth. First-order stress/displacement solid continuum reduced-integration C3D8R element is employed in the stress analysis.

The properties of the materials are given in Table 3 [30] and Table 4 [31–34]. The cutting parameters involved in simulation and experiment with representative values for scanning speed, laser power and spot diameter are listed in Table 5. These physical parameters have been experimentally proven valid through temperature measuring experiments which were described in the previous study [27].

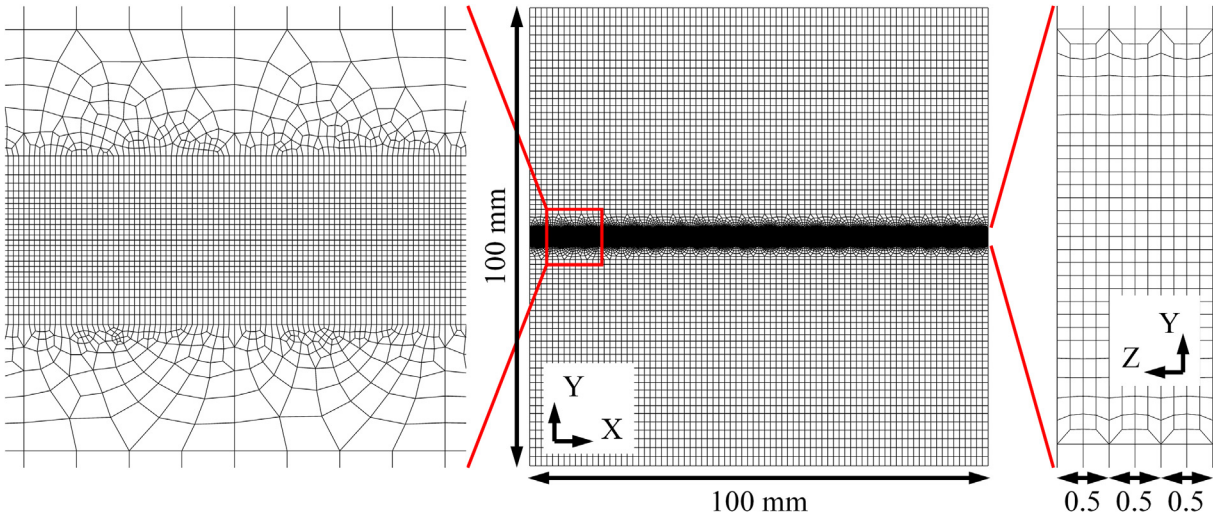

Fig. 4. Mesh geometry of the three-dimensional model of the specimen for FEM analysis.

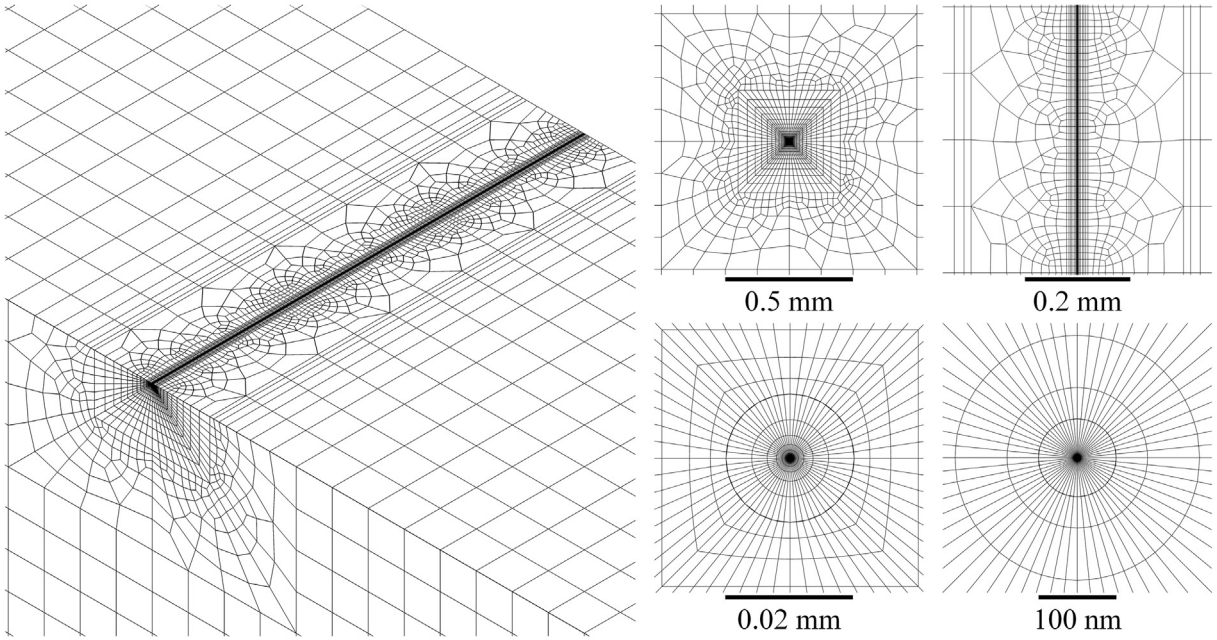

Fig. 5. Mesh geometry adjacent to the crack front region.

4. Results and discussion

4.1. FE results

Figs. 7–9 and 11 show the results of heat transfer analysis. Figs. 10, 12 and 13 show the results of thermal stress analysis.

Obviously since 99.5% of the effective energy is absorbed on the top and bottom surface of the silicon layer, and the powers of the two lasers are equal, so the highest temperature value simultaneously appears at the bonding interface at z = 0.5 and 1.0 mm on the scanning path behind the laser spot center point.

Fig. 7 shows that when the cutting speed is set at a constant value, the highest temperature value increases monotonically with increasing of time. The highest temperature value rises sharply during the beginning and ending of the cutting process and is relatively stabled around 442 °C in the middle of the cutting process. Yet, due to the heat accumulation effect near the end of the cutting path, after the laser spot reached the x = 95 mm point, the maximum temperature value could reach above BF33 glass strain point which is 518 °C. Despite the difference of the material structure, the changing regularity of the highest temperature value is in agreement with the results of the previous study [27].

Figs. 8, 9 and 11 reflect the temperature distribution from different perspective. As these figures show, all of the locations in the thickness direction in the silicon layer with the same x-coordinate and y = 0 reach its highest temperature value almost simultaneously (within 0.01 s) during the stable cutting stage. And according to the assumptions and simplifications that the temperature value of the two layers are equal at the bonding surface, so that the points on the bonding surface of both layers reach its highest temperature value simultaneously.

As Fig. 11 show, since the heat flux on the whole specimen is mirror symmetrical about z = 0.75 mm plane, the temperature distribution is also mirror symmetrical. However, the thermal loads

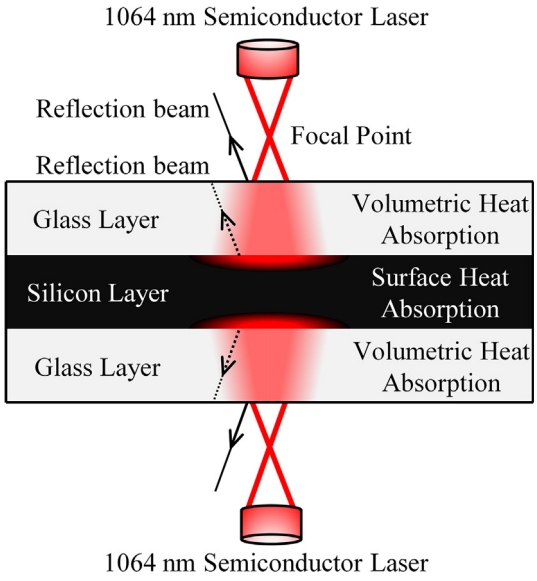

Fig. 6. Schematic of the laser irradiates the SGS wafer.

Table 2
Optical properties of BF33 glass-silicon anodic bonded wafer under 1064 nm laser radiation.

Reflectivity at the air-glass boundary [%]	3.6652
Reflectivity at the glass-silicon boundary [%]	17.0748
Absorption coefficient of glass [m^{-1}]	7.9365
Total absorption rate of glass [%]	0.3952
Absorptivity of the silicon	0.796042
Total absorption rate of Si [%]	79.6042

on the glass layer are asymmetrical in the Z-direction, the surface heat flux on the bottom surface is much greater than the volumetric heat flux inside the upper glass layer, and there is no heat source on the top surface. Also, the thermal conductivity of silicon is dozens of times than glass. So the top surface of the upper glass layer reaches its highest temperature value 0.17 s after, which means the highest temperature point is 0.51 mm behind than the

Table 5
Typical cutting parameters for simulation and experiment.

Workpiece dimensions [mm^3]	100 × 100×(0.5 + 0.5 + 0.5)
Laser power [W]	25.0 + 25.0
Scanning velocity [mm/s]	3
Laser spot diameter (mm)	3

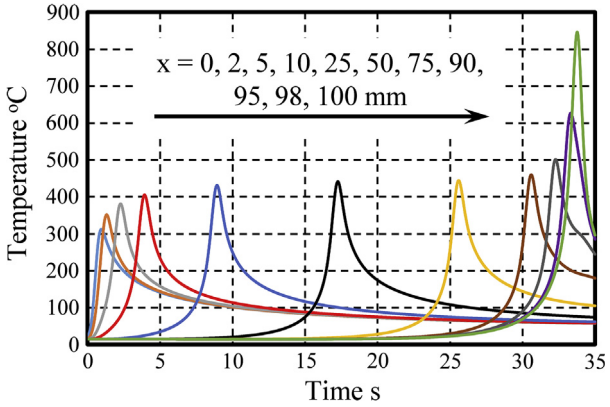

Fig. 7. Temperature versus time on the bonding interface between the upper glass layer and the silicon layer at a series of points on the scanning path defined by (x = 0, 2, 5, 10, 25, 50, 75, 90, 95, 98, 100, y = 0, z = 0.5).

point on the bottom surface, and its temperature value (394 °C at x = 50, y = 0, z = 1, t = 17.26 s) is 47 °C lower than the bottom surface (441.5 °C at x = 50, y = 0, z = 1.5, t = 17.43 s). By comparison, the temperature difference in the Z-axis direction inside the silicon layer is much small and only reaches 12 °C (430 °C at x = 50, y = 0, z = 0.75, t = 17.26 s). This value reaches 35 °C (468 °C at the bonding surface at x = 50, y = 0, z = 0.5, t = 13.08 s, and 434 °C at the exterior surface at x = 50, y = 0, z = 0, t = 13.08 s) for silicon-glass double layer wafer. Higher thermal conductivity of silicon also causes smaller temperature gradient in z-direction, higher temperature changing rate, and higher temperature before laser beam arrived and lower temperature after laser beam passed.

The thermal properties and the thermal loads could only effect the temperature distribution. In order to study the crack propaga-

Table 3
Physical properties of Borofloat 33 glass.

T [°C]	Density [kg/m^3]	Specific heat [J/kg °C]	Thermal conductivity [W/m °C]	Expansion coeff. alpha [10^{-6}/°C]	Young's modulus [GPa]	Poisson's ratio	Refractive index at 1064 nm	Fracture toughness [MPa $m^{1/2}$]	Surface energy [J/m^2]
25	2230	758	1.08	3.2	64	0.2	1.474	(0.75)	(8.0)
125	–	1071	1.25	3.2	65	0.202	–	–	–
225	–	1175	1.43	3.26	66	0.204	–	–	–
325	–	1244	1.60	3.38	67	0.206	–	–	–
425	–	1290	1.76	3.61	68	0.208	–	–	–
525	–	1325	1.92	5.7	69	0.21	–	–	–

Table 4
Physical properties of silicon.

T [°C]	Density [kg/m^3]	Specific heat [J/kg °C]	Thermal conductivity [W/m °C]	C11 [GPa]	C12 [GPa]	C44 [GPa]	Expansion coeff. alpha [10^{-6}/°C]	Refractive index at 1064 nm	Fracture toughness [MPa·$m^{1/2}$]	Surface energy [J/m^2]
25	2329	713	148.0	165.6	63.94	79.51	2.63	3.550	(0.7)	(4.0)
125	–	788	98.9	164.3	63.25	78.78	3.23	–	–	–
225	–	830	76.2	162.9	62.69	78.05	3.60	–	–	–
325	–	859	61.9	161.5	62.06	77.33	3.83	–	–	–
425	–	887	51.0	160.1	61.43	76.60	4.01	–	–	–
525	–	908	42.2	158.7	60.81	75.87	4.14	–	–	–

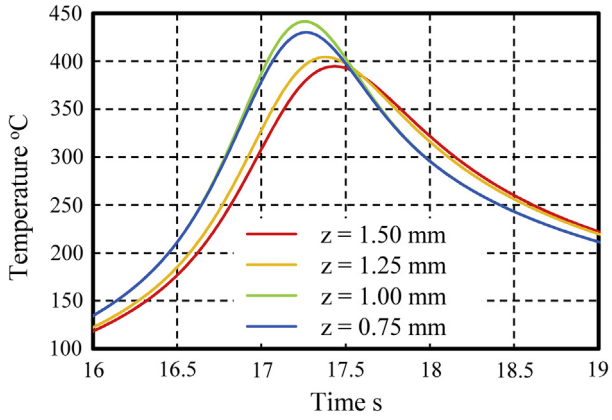

Fig. 8. Temperature versus time at a series of points on the scanning path defined by (x = 50, y = 0, z = 0.75, 1.00, 1.25, 1.50).

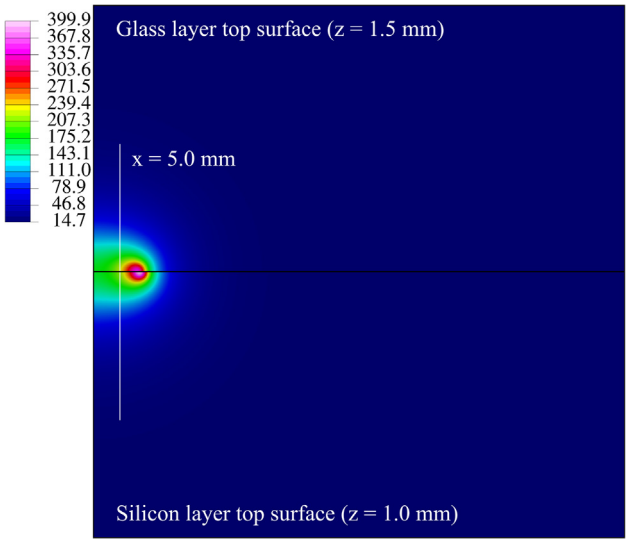

Fig. 9. Temperature distribution at t = 3.44 s on the top surfaces of the upper glass layer and silicon layer.

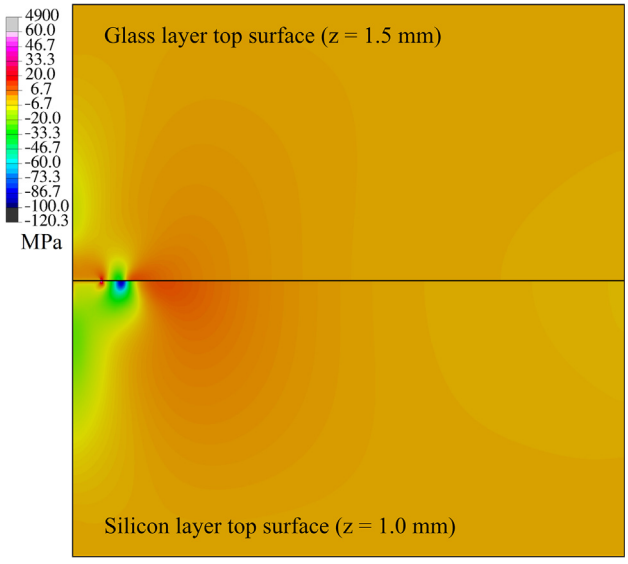

Fig. 10. Stress σ_{yy} distribution at t = 3.44 s on the top surfaces of the upper glass layer and silicon layer.

tion process, the stress distribution need to be calculated according to the temperature distribution, the thermal-mechanical properties, the geometrical shape of the materials and the mechanical boundary conditions.

Figs. 9–13 show the temperature distribution and stress σ_{yy} distribution. Due to laser induced confined thermal expansion, a compressive stress region is formed in the heating area with a lower tensile stress region ahead of the laser spot and a tensile stress region around the crack front behind the laser spot. The stress σ_{yy} has discontinuity at the bonding interface. It is assumed that the displacement at the bonding interface are identical. So, the discontinuity of the stress σ_{yy} mainly attributes to elastic difference between silicon and glass. The results show that there is hardly no stress gradient in z-direction in the silicon layer, which is much higher in both glass layers. This mainly attributes to thermal conductivity difference and asymmetrical thermal loads.

In compressive stress region, due to higher elastic modulus, maximum compressive stress σ_{yy} of −93.6 MPa is observed at the bonding interface of the silicon layer at x = 8.75 mm, z = 1.0 and 0.5 mm, and −91.9 MPa is observed in the center of the silicon layer at x = 8.75 mm, z = 0.75 mm, as shown in Figs. 10, 12 and 13. While the maximum compressive stress σ_{yy} of −64.0 MPa appears at the bonding interface of the glass layer (z = 1.0 + 0 or 0.5–0 mm), −37.9 MPa in the center of the glass layer (z = 1.25 or 0.25 mm), and −24.2 MPa on the exterior surface of the glass layer (z = 1.5 or 0.0 mm).

In tensile stress region ahead of the crack front, the stress σ_{yy} rises rapidly to the critical level. In both the glass layers, the tensile stress σ_{yy} decreases from the inner bonding surface to the exterior surface. In the silicon layer, the tensile stress σ_{yy} decreases from the center to the bonding surface. For all the layers, the stress gradient is higher near the bonding surface. In this region, with the same x-coordinate on the fracture surface, the tensile stress decreases from the inner center plane (z = 0.75 mm) to the exterior surface (z = 1.5 or 0.0 mm).

Fig. 14 shows the time history results of J-integral evaluation at the crack front across the thickness of the specimen during laser scanning. According to Eqs. (3) and (4), the crack would propagate if the J-integral value reaches 8.0 J/m^2 in the glass layer or 4.0 J/m^2 in the silicon layer. The J-integral value throughout the entire thickness of the specimen is shown to increase as the laser scanning away from the crack tip. And the J-integral value in the silicon layer is higher than the glass layer during the entire scanning process. The J-integral of the silicon layer J_S reaches critical value J_{cS} at t = 3.08 s (laser spot center arrives at x = 7.74 mm). Yet the J-integral of both glass layers J_G is only about 3.0 J/m^2. After 0.24 s (during which the laser spot travels 0.72 mm forward), J_G reaches the critical value J_{cG} at t = 3.32 s (laser spot center arrives at x = 8.46 mm). This indicates that although all the layers are separated synchronously, the crack front profile in the silicon layer is advanced than the two glass layers.

4.2. Experimental results

The preliminary feasibility experiments, including symmetrical straight line, asymmetrical straight line and circular curve cutting, are conducted under typical cutting parameters which are given in Table 5.

4.2.1. Symmetrical straight line cutting

Fig. 15 shows the optical microscope photographs of the specimen. Since the through-thickness notch has been incised on the leading edge and the crack propagation process has been effectively controlled, the cut path deviation at the leading edge is significantly reduced to merely 60 μm. All three layers of the

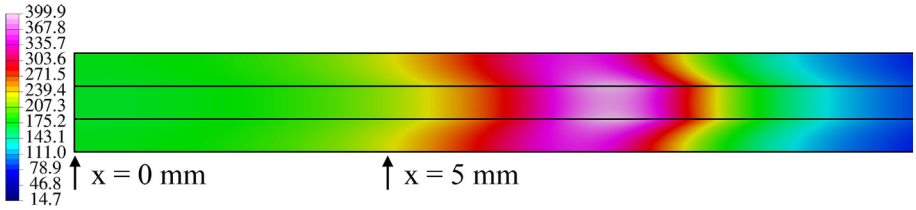

Fig. 11. Temperature distribution in x-z plane at y = 0, at t = 3.44 s.

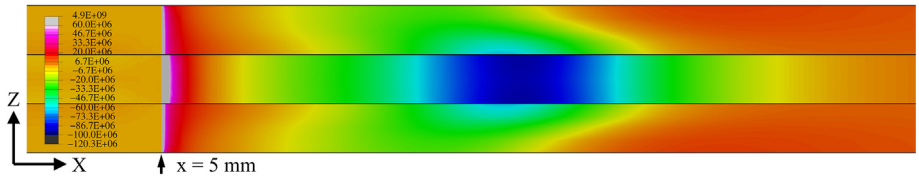

Fig. 12. Stress σ_{yy} distribution in x-z plane at y = 0, at t = 3.44 s.

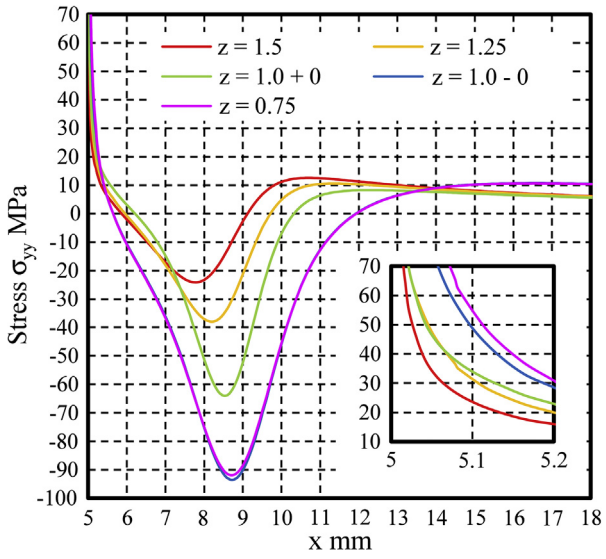

Fig. 13. Profiles of stress σ_{yy} at z = 1.5, 1.25, 1.0 + 0, 1.0–0, 0.75, y = 0 at t = 3.44 s.

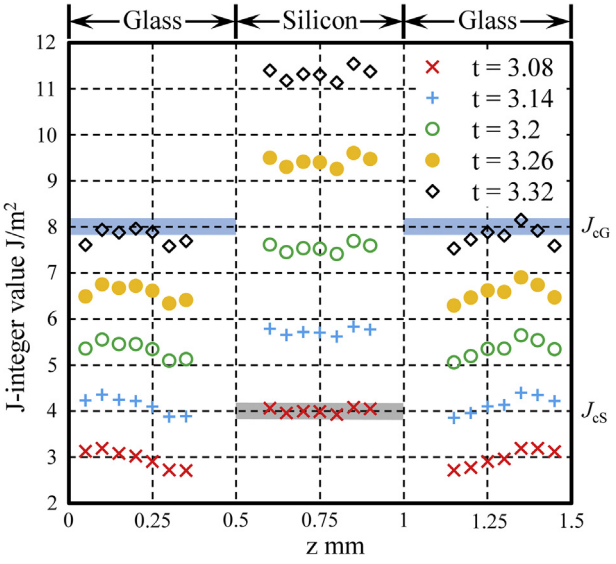

Fig. 14. J-integral value versus z-coordinate for the stationary seam-type crack when time is varied during the scanning process (no element layer excluded from the computation).

sandwich structure wafer are synchronously separated with perfect smooth fracture surface.

4.2.2. Asymmetrical straight line and circular curve cutting

Fig. 16 shows the experimental results of asymmetrical straight line cutting. The wafer did not fully separated immediately after the cutting process. The distance between the right side boundary of the wafer and the scanning path is only 6.78 mm, which means the materials on two sides of the scanning path are asymmetrical. In asymmetrical straight line cutting conditions, the constraints provided by the surrounding materials are also asymmetrical, which would finally cause an uneven stress distribution near the crack tip. This means the fracture mode of the crack is not pure mode I. The whole fracture path appears as a bow-shaped arc bending to the left side. The similar results could also be expected during single layer glass, silicon or ceramics asymmetrical cutting. The maximum deviation between the fracture path and the scanning path reaches 0.6 mm. And due to constrained thermal expansion effect at the final moment, the materials would reach even higher temperature and expand much more. However, there is no more materials ahead to provide high enough compression. Therefore the crack would open rapidly. Result shows the crack opening displacement (COD) reached 0.56 mm at the leading edge.

Fig. 17 shows the experimental results of circular curve cutting. The scanning path consist of a straight line and a circular curve with 30.00 mm radius. The fracture path generally followed the scanning path. The path deviation at the leading edge could easily be seen. But the error between the fracture path and the geometrical circular arc curve is under 70 μm.

As Fig. 17 illustrates, the COD is only 107 μm, which is less than 1/5 of the COD result of asymmetrical straight line cutting experiment. This is because the orientation of the fracture path changes during the circular curve cutting section, and the total scanning path length is 51.843 mm, which is only half length of the scanning path in the asymmetrical straight line cutting.

4.2.3. Cutting quality and crack propagation process analysis

Fig. 18 shows the optical microscope photograph of the fracture surface. The crack propagation profiles, which appear similar to Wallner lines, could be found on the silicon layer and on both

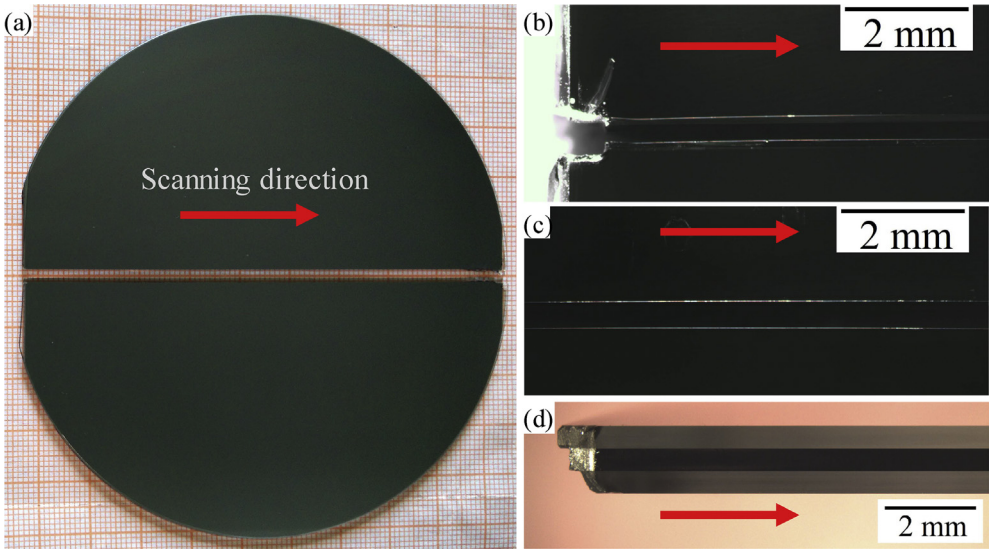

Fig. 15. Photographs of the specimen: (a) the whole specimen, (b) cut path deviation at the leading edge, (c) the cutting path on the upper glass layer side, (d) fracture surface of the left half wafer at the leading edge.

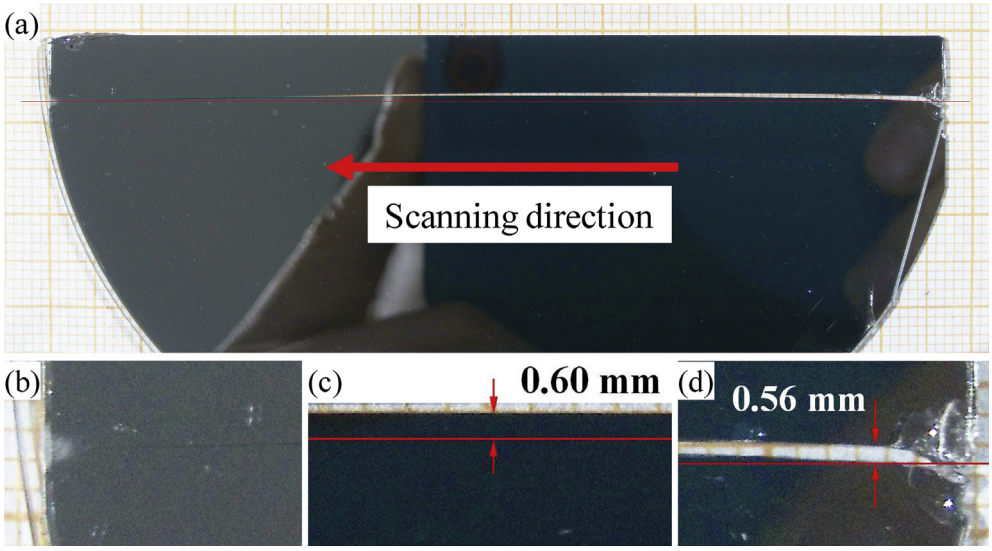

Fig. 16. Photographs of the specimen after asymmetrical straight line cutting (a) wafer just being cut but not fully separated, (b) not fully separated cutting path at the trailing edge, (c) maximum deviation occurs near the middle of cutting path, (d) crack opening at the leading edge.

the glass layers near to the bonding interface. These regular ripple-like cleavage step lines on the fracture surface represent the changing history of the crack tip positions during the cutting process. The red/blue curve represents a crack front at a certain time that the upper/lower glass layer and the silicon layer fractured simultaneously.

Studies show that the cleavage steps lines on the fracture surface of single layer silicon [20–22,35] are C-shaped or L-shaped (laser radiates on the top surface). Regarding single layer glass under full body cutting, studies show no cleavage steps. However, since the glass is transparent, the crack front shape can be captured by a camera during the cutting process. And according to the simulation and the experiments results acquired by Zhao [36,37], the crack front of glass is C-shaped. For single layer sheet, the immediate cause of the formation of the C-shaped crack front profile is the stress distribution, which is strongly influenced by air convection on exterior surface, the thickness of the sheet and the absence of constraint brings by surrounding materials, such as surface films.

However, for the SGS wafer, the boundary conditions and constraints are completely different. The cleavage steps on the fracture surfaces of the upper glass layer, the middle silicon layer and the lower glass layer are L-shaped, reverse C-shaped and Γ-shaped, respectively. In the area which is far from the bonding surface of the glass layer ($z > 1.25$ or $z < 0.25$ mm roughly), the fracture surface is smooth and the step lines could hardly be seen. These cleavage step lines indicate that the crack propagation profile in the silicon layer is ahead of the glass layers. The length in the X-direction of a single crack propagation profile is about 0.35 mm, which is accordance with the tensile stress distribution and the J-integral value gained by FE analysis.

Fig. 19 shows the SEM image from the fracture surface at the bonding surface. There is no debonding, chipping or micro-cracks

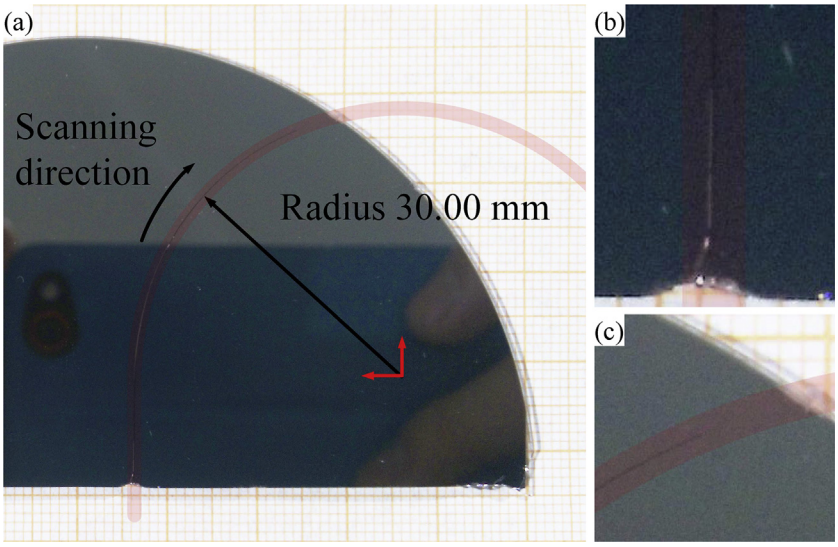

Fig. 17. Photographs of the specimen after circular curve cutting: (a) wafer just being cut but not fully separated, (b) cut path deviation at the leading edge, (c) not fully separated cutting path at the trailing edge.

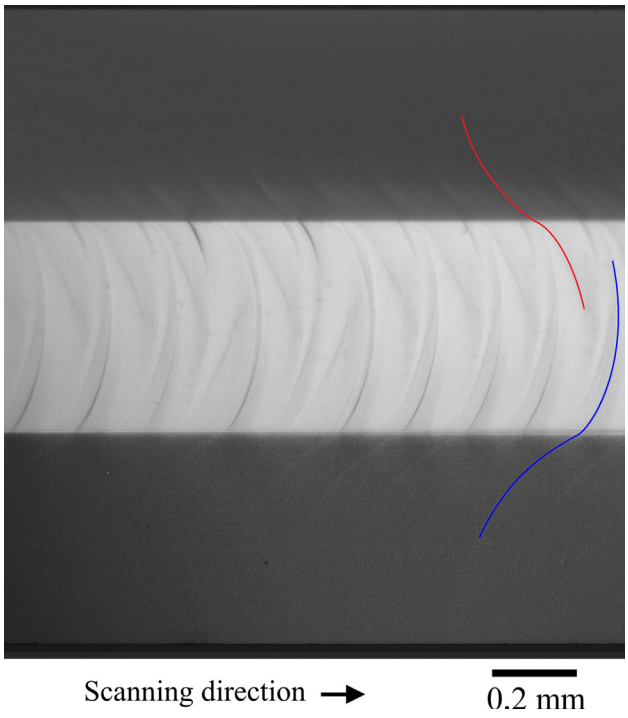

Fig. 18. Crack propagation profile from the fracture surface (contrast and brightness of the glass layer area has been adjusted to make the crack propagation profile more identifiable).

on the fracture surface near the bonding interface. Figs. 20 and 21 show the measurement results of the fracture surface profile at the center of the upper glass and silicon layer. Apparently, the fracture surface of the glass layer is locally smoother than the silicon layer. And the fracture surface profile curve of the silicon layer is cyclical, which means crack propagates discontinuously. This is because silicon is anisotropic elastic and brittle, and the cutting speed and the crack growth rate could differ by orders of magnitude. Even so, the overall fracture surface is flat and smooth with an average roughness Ra under 1 μm.

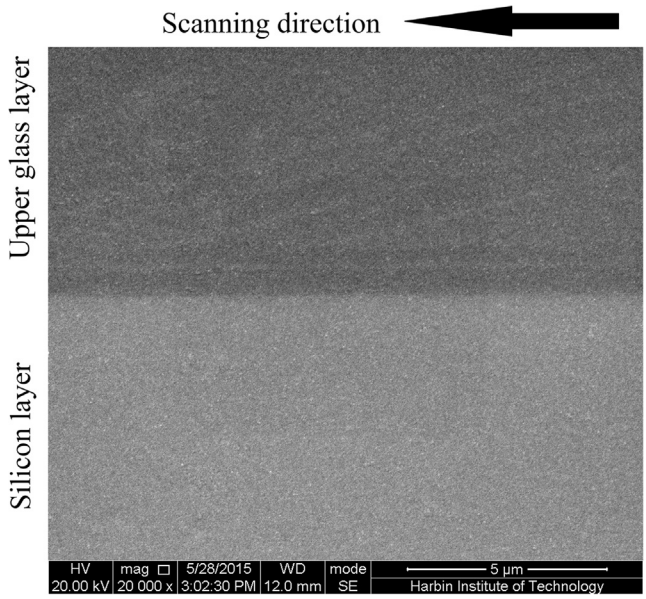

Fig. 19. SEM image of the fracture surface at the bonding surface.

5. Conclusions

The LITP technique was successfully applied to the cutting of SGS wafer. Considering the geometric symmetry of the sandwich structure wafer, the authors designed the laser system containing double laser beams and created a symmetrical temperature stress field in the wafer. A sound three-dimensional simulation model capable of representing the essential physical processes of the sandwich structure wafer under laser radiation was proposed and J-integral value at the crack tip was calculated. A set of typical processing parameters (overall laser power is 50 W (25.0 + 25.0 W), spot diameter is 3 mm, and scanning speed is 3 mm/s) was adopted in the simulation and the experiments. The mechanism of 1064 nm laser cutting SGS wafer using LITP method was investigated, and the crack propagation profile is explained by the tensile thermal-stress distribution and the J-integral value.

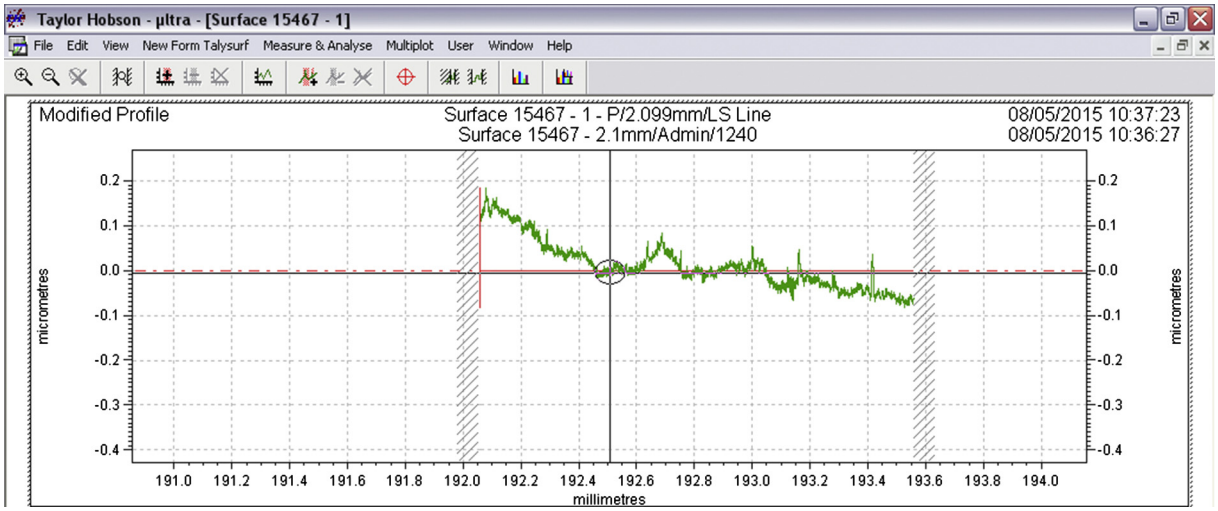

Fig. 20. Fracture surface profile in the middle section of the cutting path at the center of the upper glass layer (z = 1.25 mm).

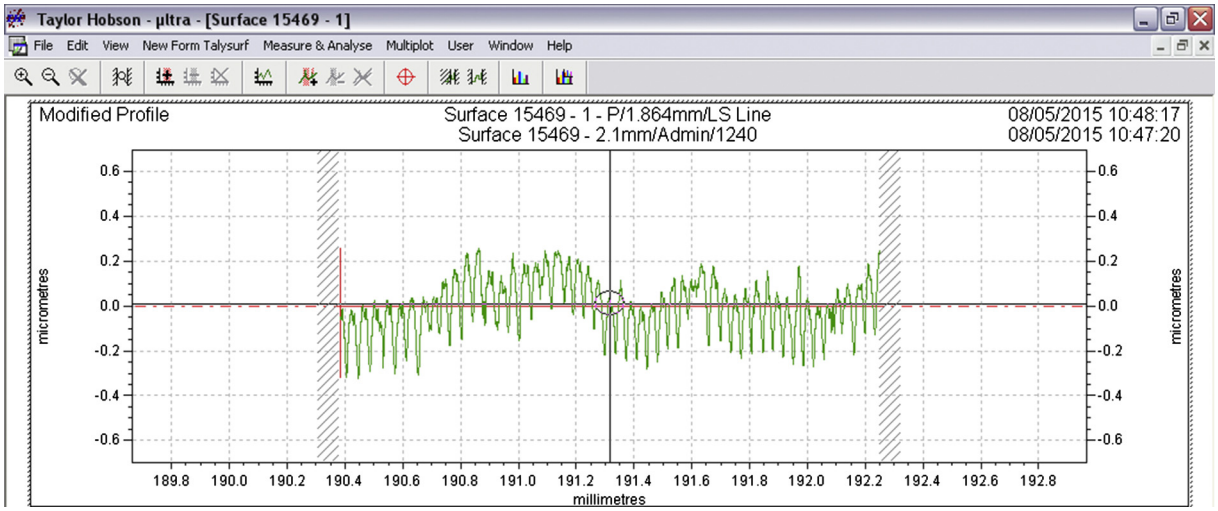

Fig. 21. Fracture surface profile in the middle section of the cutting path at the center of the silicon layer (z = 0.75 mm).

The results presented in this paper are important for understanding the crack propagation process in laser cutting sandwich structure wafer. The authors expect that there will be further developments of the technique in terms of the optimization of the cutting parameters, the cutting of multiple cells wafer and the method for generating trigger crack et al.

Acknowledgments

This research is supported by the National Natural Science Foundation of China (No. 51275118, No. 51275117), National 863 project (No. 2015AA042702), authors gratefully acknowledge their support.

References

[1] K.M. Knowles, A.T.J. Van Helvoort, Anodic bonding, Int. Mater. Rev. 51 (5) (2006) 273–311.
[2] L.D. Stefano, K. Malecki, F.G.D. Corte, et al., A microsystem based on porous silicon-glass anodic bonding for gas and liquid optical sensing, Sensors 6 (6) (2006) 680–687.
[3] Y. Luo, G. Liu, L. Zou, B. Yu, X. Wang, Thermal behavior investigation of silicon-pyrex micro heat pipe, Aip Adv. 4 (3) (2014) 32–33.
[4] T. Zhang, H. Zhang, J. Xu, S. Liu, Z. Gan, Study on triple-stack anodic bonding using two electrodes, Sens. Actuat., A 157 (1) (2010) 168–172.
[5] Y. Zhang, G. Yang, C. Gao, et al., A MEMS sandwich differential capacitive silicon-on-insulator accelerometer, Microsyst. Technol. 19 (8) (2013) 1249–1254.
[6] M. Esashi, Wafer level packaging of MEMS, J. Micromech. Microeng. 18 (7) (2008).
[7] Miyake. Yasuaki, Separation technology for FPD glass, J. Japan Soc. Abrasive Technol. 45 (7) (2001) 342–347.
[8] A. Riveiro, F. Quintero, F. Lusquinos, Study of melt flow dynamics and influence on quality for CO_2 laser fusion cutting, J. Phys. D 44 (13) (2011) 135501–135513.
[9] N. Sudani, K. Venkatakrishnan, B. Tan, Laser singulation of thin wafer: die strength and surface roughness analysis of 80 µm silicon dice, Opt. Lasers Eng. 47 (7) (2009) 850–854.
[10] K. Wlodarczyk, A. Brunton, P. Rumsby, Picosecond laser cutting and drilling of thin flex glass, Opt. Lasers Eng. 78 (2016) 64–74.
[11] D. Perrottet, A. Spiegel, F. Wagner, Particle-free semiconductor cutting using the water jet guided laser, Proc. SPIE 5713 (1) (2005) 240–246.
[12] R.M. Lumley, Controlled separation of brittle materials using a laser, Am. Ceram. Soc. Bull. 48 (1969) 850–854.
[13] K. Karube, N. Karube, Laser-induced cleavage of LCD glass as full-body cutting, Proc. SPIE 6880 (1) (2008).
[14] L. Yang, Y. Wang, Z. Tian, YAG laser cutting soda-lime glass with controlled fracture and volumetric heat absorption, Int. J. Mach. Tools Manuf 50 (10) (2010) 849–859.
[15] Y. Miyashita, M. Mogi, H. Hasegawa, Study on a controlling method for crack nucleation and propagation behavior in laser cutting of glass, J. Solid Mech. Mater. Eng. 2 (12) (2008) 1555–1566.

[16] S. Nisar, M.A. Sheikh, L. Li, S. Safadar, Effect of thermal stresses on chip-free diode laser cutting of glass, Opt. Laser Technol. 41 (2009) 318–327.
[17] Y.Z. Wang, J. Lin, Characterization of the laser cleaving on glass sheets with a line-shape laser beam, Opt. Laser Technol. 39 (2007) 892–899.
[18] K. Huang, W. Hsiao, C. Hwang, The laser ablation model development of glass substrate cutting assisted with the thermal fracture and ultrasonic mechanisms, Opt. Lasers Eng. 67 (2015) 31–35.
[19] C. Su, Y. Hsiao, C. Chang, Parameter optimization design for touch panel laser cutting process, IEEE Trans. Autom. Sci. Eng. 9 (2) (2012) 320–329.
[20] K. Yamada, T. Ueda, A. Hosokawa, Thermal damage of silicon wafer in thermal cleaving process with pulsed laser and CW laser, Proc. SPIE 6107 (1) (2006).
[21] T. Ueda, K. Yamada, K. Oiso, Thermal stress cleaving of brittle materials by laser beam, Cirp Ann. – Manuf. Technol. 51 (1) (2002) 149–152.
[22] J. Liu, J. Lu, X. Ni, Pulsed Nd:YAG laser cutting of silicon wafer by controlled fracture technique, Proc. SPIE 7843 (2010) 784318.
[23] L. Yang, Y. Wang, Z. Tian, Laser cutting ZrO_2 ceramic with controlled fracture technique, IEEE Int. Conf. Mechatron. Autom. (2012) 1272–1276.
[24] D.B. Xiao, X. Zhang, Z.Q. Hou, X.Z. Wu, et al., UV laser dicing without failure caused by contamination and heat for thick anodically bonded silicon/glass MEMS wafers., Solid-State Sens., Actuat. Microsyst. Conf. (2011) 2339–2342.
[25] Y. Izawa, S. Tanaka, H. Kikuchi, Y. Tsurumi, N. Miyanaga, M. Esashi, et al., Debris-free in-air laser dicing for multi-layer MEMS by perforated internal transformation and thermally-induced crack propagation, IEEE International Conference on Micro Electro Mechanical Systems, vol. 2008, IEEE, 2008, pp. 822–827.
[26] D.B. Xiao, Q.S. Li, Z.Q. Hou, et al., A novel sandwich differential capacitive accelerometer with symmetrical double-sided serpentine beam-mass structure, J. Micromech. Microeng. 26 (2) (2016) 025005.
[27] Y.C. Cai, L.J. Yang, H.Z. Zhang, Y. Wang, Laser cutting silicon-glass double layer wafer with laser induced thermal-crack propagation, Opt. Lasers Eng. 82 (2016) 173–185.
[28] J. Rice, Path independent integral and the approximate analysis of strain concentration by notches and cracks, J. Appl. Mech. 35 (1968) 379–386.
[29] Brian. Lawn, Fracture of Brittle Solids, second ed., Cambridge University Press, 1993.
[30] Schott Borofloat 33. SCHOTT North America, Inc., <http://www.us.schott.com/borofloat>, 2015.
[31] Veikko. Lindroos, Handbook of Silicon Based MEMS Materials and Technologies, Elsevier, 2010.
[32] A. Masolin, P.O. Bouchard, R. Martini, Thermo-mechanical and fracture properties in single-crystal silicon, J. Mater. Sci. 48 (3) (2013) 979–988.
[33] Watanabe Hiromichi, Yamada Naofumi, Okaji Masahiro, Linear thermal expansion coefficient of silicon from 293 to 1000 K, Int. J. Thermophys. 25 (1) (2004) 221–236.
[34] Martin A. Green, Self-consistent optical parameters of intrinsic silicon at 300 K including temperature coefficients, Sol. Energy Mater. Sol. Cells 92 (11) (2008) 1305–1310.
[35] C.Y. Zhao, H.Z. Zhang, Y. Wang, Research on laser induced thermal-crack propagation cutting silicon wafer, Adv. Mater. Res. 628 (2013) 211–217.
[36] C.Y. Zhao, H.Z. Zhang, Y. Wang, Semiconductor laser asymmetry cutting glass with laser induced thermal-crack propagation, Opt. Lasers Eng. 63 (2014) 43–52.
[37] C.Y. Zhao, H.Z. Zhang, L.J. Yang, Dual laser beam revising the separation path technology of laser induced thermal-crack propagation for asymmetric linear cutting glass, Int. J. Mach. Tools Manuf 106 (2016) 43–55.